Partitioning and Coarsening Dynamics of Precipitate-Strengthened Cr-Si Alloys: The Role of Ge, Pt, and Mo

Anke Silvia Ulrich,* Petra Pfizenmaier, Michael Kerbstadt, Lucas Pelchen, Ali Solimani, Uwe Glatzel, and Mathias Christian Galetz

Cr solid solution (Cr_{ss}) alloys strengthened by A15-phase precipitates (e.g., Cr_3Si) are promising candidates for high-temperature structural materials. A series of Cr-base alloys (Cr $\geq$ 89 at%) with strengthening A15-phase precipitates consisting of up to five alloying elements is investigated. Scanning electron microscopy with energy-dispersive X-ray spectroscopy, electron probe microanalysis with wavelength-dispersive X-Ray spectroscopy, X-ray diffraction, image analysis, and nano- and microindentation are used to characterize the interplay of alloying elements on hardness, microstructural partitioning, and coarsening behavior when annealed for 400 h at 1050 °C, 100 h at 1200 °C, and 100 h at 1350 °C. The impact of the alloying elements on microstructure is found to be combinatory in the investigated composition space, independent of the compositional complexity of the alloy. Ge and especially Pt enhance microstructural coarsening, while Mo additions can counteract this. Ge and Pt mainly partition in the A15 phase, while Mo equally partitions in both phases. Partitioning of Pt depends on the overall alloy composition, which is the reason for enhanced precipitate coarsening. Considering the different partitioning behaviors of individual elements, a collective parameter (Si equivalent (Si_{eq})) is introduced in this work to formulate the impact of additional alloying elements on the microstructural evolution of such Cr-base alloys.

1. Introduction

Cr-rich alloys strengthened by A15-phase precipitates are promising structural materials for high-temperature applications in aerospace and fusion applications. Their melting point ranges

A. S. Ulrich, P. Pfizenmaier, L. Pelchen, U. Glatzel
Metals and Alloys
Faculty of Engineering Science
University of Bayreuth
Prof.-Rüdiger-Bormann-Str. 1, 95447 Bayreuth, Germany
E-mail: silvia.ulrich@uni-bayreuth.de

M. Kerbstadt, A. Solimani, M. C. Galetz
High Temperature Materials
DECHEMA-Forschungsinstitut
Theodor-Heuss-Allee 25, 60486 Frankfurt, Germany

from 1715 °C to around 1900 °C, potentially offering higher application temperatures as in aerospace or chemical and petrochemical industries commonly used Ni-based (super)alloys.[1,2] Cr-Si-based alloys show good tensile and creep strengths at high temperatures and high resistivity against oxidation and corrosion.[3–6] Due to their high oxidation resistance to steam, they are also considered promising for nuclear applications.[7]

Materials considered for high-temperature applications require alloys with a toughening matrix, which facilitates fabrication and reduces brittleness with an embedded strengthening phase and sufficient resistance to the surrounding environment. Accordingly, Cr-rich Cr-Si alloys consisting of a bcc Cr solid solution A2-matrix (Cr_{ss}) and hard, strengthening Cr_3Si-A15-precipitates are particularly interesting.

Cr-Si alloys provide low densities ($\rho(Cr) = 7.2 \times 10^{-3}\,\mathrm{kg\,cm^{-3}}$, lower in comparison to Ni-based materials with $\rho(Ni) = 8.9 \times 10^{-3}\,\mathrm{kg\,cm^{-3}}$), high availability, and low supply risks of the base metals,[8,9] and Si and Cr are among the most favorable oxide formers at high temperatures. On the contrary, pure Cr and Cr-rich alloys suffer from impurity-enhanced low ductility, high ductile to brittle transition temperatures (DBTT) much above room temperature, and a pronounced notch sensitivity.[10,11]

This study considers alloys with a Cr_{ss} matrix and A15 precipitates capable of varying the A15-phase fraction by respective heat treatments. Alloy compositions with at least 89 at% Cr are considered, because Si concentrations $c(Si)$ higher than the eutectic composition ($c(Si) = 16$ at%) form an A15 matrix, leading to pronounced embrittlement. Additionally, above around $c(Si) = 11$ at% eutectic regions occur, which is considered unfavorable for the mechanical properties.[6,12] Si was found to improve the oxidation and nitridation resistance of Cr-based alloys significantly.[13,14] The solubility limit of Si in Cr_{ss} was found to be 4.8–7.1 at% in the temperature range of 1050–1350 °C; hence, higher A15-phase former concentrations are chosen in this study to maintain the two-phase microstructure.[6,12,15] In addition, $Cr_{91}Si_9$ was reported to produce a high A15-phase fraction by simultaneously avoiding eutectic regions.[6] Focusing on the Cr_{ss}-A15-system, ternary alloying of Ge, Mo, or Pt improved the alloy's high-temperature performance further while

simultaneously maintaining the two-phase microstructure ($Cr \geq 89$ at%).[16–18] Ge enhances oxidation resistance and decreases scale spallation.[19,20] Substituting 2 at% of Si by Ge was found to improve the nitridation and oxidation resistance by simultaneously maintaining a fine microstructure.[21–23] Mo and Pt improve nitridation resistance.[24–26] To systematically investigate the elemental influences, also 2 at% Si is substituted by Mo and Pt to obtain ternary compositions. Mo additionally improves creep properties, and recently, it was shown that adding Mo decreases the DBTT for Cr-rich alloys.[27–29] Additionally, an improvement of nitration resistance by substituting 2 at% Cr by Mo was reported while substituting 5 or 20 at% increases the attack again by enhanced MoO_3 evaporation.[24,30] Recent studies support the findings of Rudy and Nowotny that a brittle σ-phase exists in the Cr_{ss}-A15 two-phase region at temperatures around 1300 °C.[31] Cr alloys with high Mo concentrations, for example, $Cr_{54.3}Si_{13.5}Mo_{32.2}$ or $Cr_{67}Mo_{25}Si_8$, are not suitable for casting, as they form brittle σ-phase upon cooling.[24,26] Based on these findings and previously published investigations, the concentration of Mo is limited to a maximum of 2 at% in the current study. Substituting 2 at% Si by Pt was found to improve oxidation and nitridation resistance, but higher amounts up to 6 at% were found to cause enhanced coarsening.[18,25] This is why a maximum concentration of 2 at% Pt is chosen in this work. For the quaternary and quinary alloys, the most oxidation-resistant $Cr_{91}Si_7Ge_2$ alloy is chosen as reference,[25] and Mo and Pt were added at the expense of Cr. For an additional comparison to the quaternary systems, the Cr, Si, and Ge concentrations are kept constant in the investigated quinary $Cr_{89}Si_7Ge_2Pt_1Mo_1$ alloy. The study focuses on the microstructures evolved at 1200 °C. The findings are supplemented by microstructural investigations of selected alloy compositions after annealing at 1050 and 1350 °C. The temperatures 1050, 1200, and 1350 °C are chosen for the heat treatments as they are in the range of possible future application temperatures and are either comparable to extreme conditions for Ni-based superalloys or higher. The length of annealing is chosen to be 100 h for 1200 and 1350 °C which offers the possibility to reach phase compositions close to thermodynamic equilibrium.[6] For annealing at 1050 °C, pre-experiments on binary alloys showed the necessity of a prolonged annealing time of 400 h.

This study meets the scientific question of whether the positive, element-depending effects reported for the ternary compositions could be maintained and combined in more complex systems. The study is motivated by the fact that conventional high-temperature alloys such as Ni-based superalloys consist of up to 10 alloying elements (trace elements not considered), each one serving a specific effect that is maintained in its combination. This work investigates the impact of combining the alloying elements Si, Ge, Pt, and Mo in Cr-rich alloys on microstructure, phase evolution, and stability.

2. Experimental Section

2.1. Alloy Manufacturing

The alloys were prepared by arc melting of 7×10^{-3} kg or 30×10^{-3} kg ingots with diameters of around 1×10^{-2} m. Cr pieces (Cr > 99.95 wt%, Plansee), Si pieces (Si > 99.999 wt%,

GfE), Ge pieces (Ge > 99.999 wt%, Haines & Maassen), Mo wire (Mo > 99.97 wt%, Plansee), and Pt pieces (Pt > 99.9 wt%, Hereaus) were used as raw materials. Melting of the ingots was conducted under a high-purity argon atmosphere in a compact arc melter (MAM-1, Edmund Bühler, Germany) on a water-cooled copper mold. Before melting the aimed compositions, a Zr oxygen getter was melted twice. The cast ingots were remelted five times during processing. The measured purity of the alloys after arc-melting was 99.936 wt% with $C \approx 16$ ppm, $N \approx 12$ ppm, $O \approx 154$ ppm, $S < 5$ ppm, $Al < 10$ ppm, $Fe \approx 64$ ppm, $Cu < 5$ ppm, and $Zr \approx 384$ ppm (determined using hot gas extraction, combustion analysis in O_2, and optical emission spectroscopy for a $Cr_{91}Si_7Ge_2$ alloy after arc-melting).[30]

The ingots were cut into specimens with dimensions around $ø10 \times 10^{-3}$ m and 8×10^{-3} m in length and a planar surface (around 1×10^{-4} m²) parallel to the solidification direction using wire erosion. The alloys were heat treated for either 400 h at 1050 °C (cut from 30 g ingot), 100 h at 1200 °C (cut from 7 g ingot), or 100 h at 1350 °C (cut from 30 g ingot). Each sample was separately encapsulated in an evacuated and sealed quartz glass tube (inner $ø12 \times 10^{-3}$ m and a length of maximum 12×10^{-2} m) in a muffle furnace (experiments at 1200 °C: Nabertherm HTC 03/15; experiments at 1050 and 1350 °C: Nabertherm LHT 04/18). Prior to annealing, leftovers of the cutting process were removed by wet grinding up to P320 grit (ANSI). After this heat treatment, the samples were quenched in water by simultaneously destroying the quartz glass tubes using pliers. Heat treatment curves are provided in **Figure 1**.

2.2. Microstructural Investigations

The annealed samples were mounted in epoxy resin with their cross section face up. The microstructural investigations were conducted on the ingot's cross sections representing the microstructure parallel to the solidification direction. All cross sections were ground to a final surface finish of 1 μm using SiC papers (P120–P1000 grit (ANSI)) and diamond suspensions (3 and 1 μm). Afterward, X-Ray diffraction (XRD, Cu-K$_\alpha$ radiation) was conducted on the cross sections to determine phases (Bruker D8 advance diffractometer). 2θ was varied from 20 to 90° with a step size of 0.02° and 4 s measurement time per step. Lattice parameters were calculated based on the XRD data using the Nelson–Riley (NR) extrapolation function (Diffrac.EVA software).[32] The microstructural appearance was investigated using optical microscopy, scanning electron microscopy (SEM, Philips XL40 electron microscope) equipped with an energy-dispersive X-Ray spectrometer (EDS), and electron probe microanalysis (EPMA, JEOL JXA-8100) equipped with wavelength-dispersive X-Ray spectrometer (WDS). EPMA backscattered electron images (BSE) and semiquantitative EPMA element distribution maps were recorded using an acceleration voltage of 1.5×10^2 V.

For investigating the microstructural evolution, quantitative EPMA spot measurements were conducted in an 11×11 grid with a step size of 1 μm in the center of the specimens. Four SEM-EDS area measurements (50×50 μm, 20 kV) were additionally conducted over the whole cross section to investigate the homogeneity of the alloy composition. To determine the

**ADVANCED
SCIENCE NEWS**

www.advancedsciencenews.com

**ADVANCED
ENGINEERING
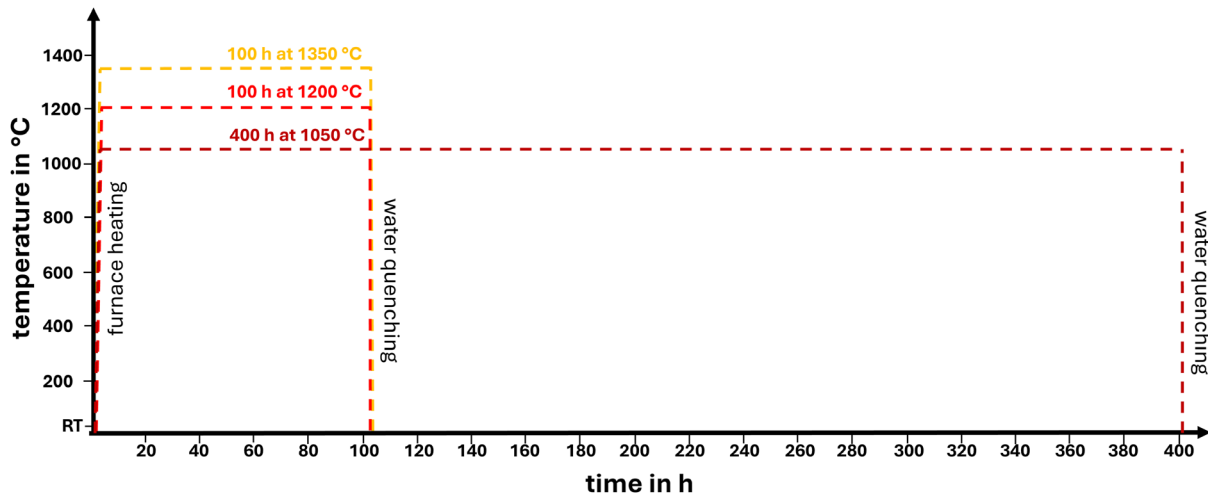MATERIALS**

www.aem-journal.com

Figure 1. The displayed curves show the temperature over time for the three different heat treatments used in this work.

area fraction of formed A15 precipitates in the Cr_{ss} matrix, Si element maps were analyzed using ImageJ 1.51 software.[33] Therefore, at least four Si element maps were measured at different positions. For the investigations of the microstructures after annealing, a magnification of 1000× was used. However, the alloys annealed at 1200 °C were investigated using EPMA/WDS while the at 1050 and 1350 °C annealed samples were measured using SEM/EDS. Therefore, the values are not directly compared.

Electron backscatter diffraction (EBSD, Hikari Super EBSD Camera, Zeiss Sigma 300 VP) was used to measure the grain size at magnifications of 30× to 80× depending on the grain size determined. Only data points with a confidence index greater than 0.5 and uncut grains were used to analyze the data. Due to anisotropic grain shapes in the samples, the grain size was valued by using the minor and major axis diameter of the elliptical grains in addition to the average grain size.

2.3. Hardness Measurements

Hardness measurements were conducted on the center of the cross sections at room temperature. The hardness of the individual phases, the Cr_{ss} matrix, and the A15 precipitates were determined by nanoindentation, while the overall alloy's hardness was determined by Vickers' method (HV0.3). The nanoindentation tester NHT2 (CSM Instruments, Switzerland) equipped with a Berkovich tip was used and the measurements were carried out under a constant load of 2×10^{-2} N. A loading rate of 0.67×10^{-3} Ns^{-1} and an unloading rate of 1.3×10^{-3} Ns^{-1} were used. The indentation hardness HIT is an average value of at least six measurements. More detailed information on the determination of the nanoindentation hardness using this method and a Berkovich can be found elsewhere.[34] Microhardness measurements were conducted using the M-400-H Leco microhardness testing device equipped with a Vickers diamond pyramid indenter, a load of 0.3 kg, and a dwell time of 15 s.

3. Results

3.1. Effects of Alloying on Phases and Compositions

The investigated alloys in this study and their nominal compositions are listed in **Table 1**. All materials were manufactured by arc melting. The values are given for the samples after annealing for 100 h at 1200 °C determined by EPMA point measurements. Measurements for the binary compositions, $Cr_{91}Si_7Ge_2$, $Cr_{90}Si_8Mo_2$, and $Cr_{91}Si_7Pt_2$ were already published in a former study as the same ingots were used.[15]

In **Figure 2**, the microstructures of the alloys after annealing for 100 h at 1200 °C are shown. All alloys form a two-phase structure consisting of a Cr_{ss} and a Si-rich A15-phase. The different contrast between the matrix and the precipitates depending on the alloy composition is striking in the microstructures shown in Figure 2.

Table 1. Measured compositions of the investigated alloys and corresponding alloy labels. The values of the binary and ternary compositions are reproduced with permission.[15] Copyright 2024, Elsevier.

Nominal composition	c(Cr) in at%	c(Si) in at%	c(Ge) in at%	c(Mo) in at%	c(Pt) in at%
$Cr_{93}Si_7$	93.2 ± 0.3	6.6 ± 0.3	–	–	–
$Cr_{92}Si_8$	92.0 ± 0.2	7.9 ± 0.2	–	–	–
$Cr_{91}Si_9$	90.9 ± 0.3	9.1 ± 0.3	–	–	–
$Cr_{90}Si_{10}$	90.0 ± 0.4	9.6 ± 0.4	–	–	–
$Cr_{91}Si_7Ge_2$	90.7 ± 0.2	7.0 ± 0.1	2.2 ± 0.2	–	–
$Cr_{90}Si_8Mo_2$	89.9 ± 0.6	7.8 ± 0.5	–	2.0 ± 0.1	–
$Cr_{91}Si_7Pt_2$	90.9 ± 0.3	6.7 ± 0.2	–	–	2.1 ± 0.1
$Cr_{89}Si_7Ge_2Mo_2$	88.6 ± 0.5	7.1 ± 0.4	2.0 ± 0.2	2.0 ± 0.1	–
$Cr_{89}Si_7Ge_2Pt_2$	89.0 ± 0.7	6.7 ± 0.5	2.0 ± 0.3	–	2.1 ± 0.1
$Cr_{89}Si_7Ge_2Mo_1Pt_1$	88.0 ± 0.9	7.5 ± 0.8	2.3 ± 0.1	1.1 ± 0.1	1.1 ± 0.2

**ADVANCED
SCIENCE NEWS**

www.advancedsciencenews.com

**ADVANCED
ENGINEERING
MATERIALS**

www.aem-journal.com

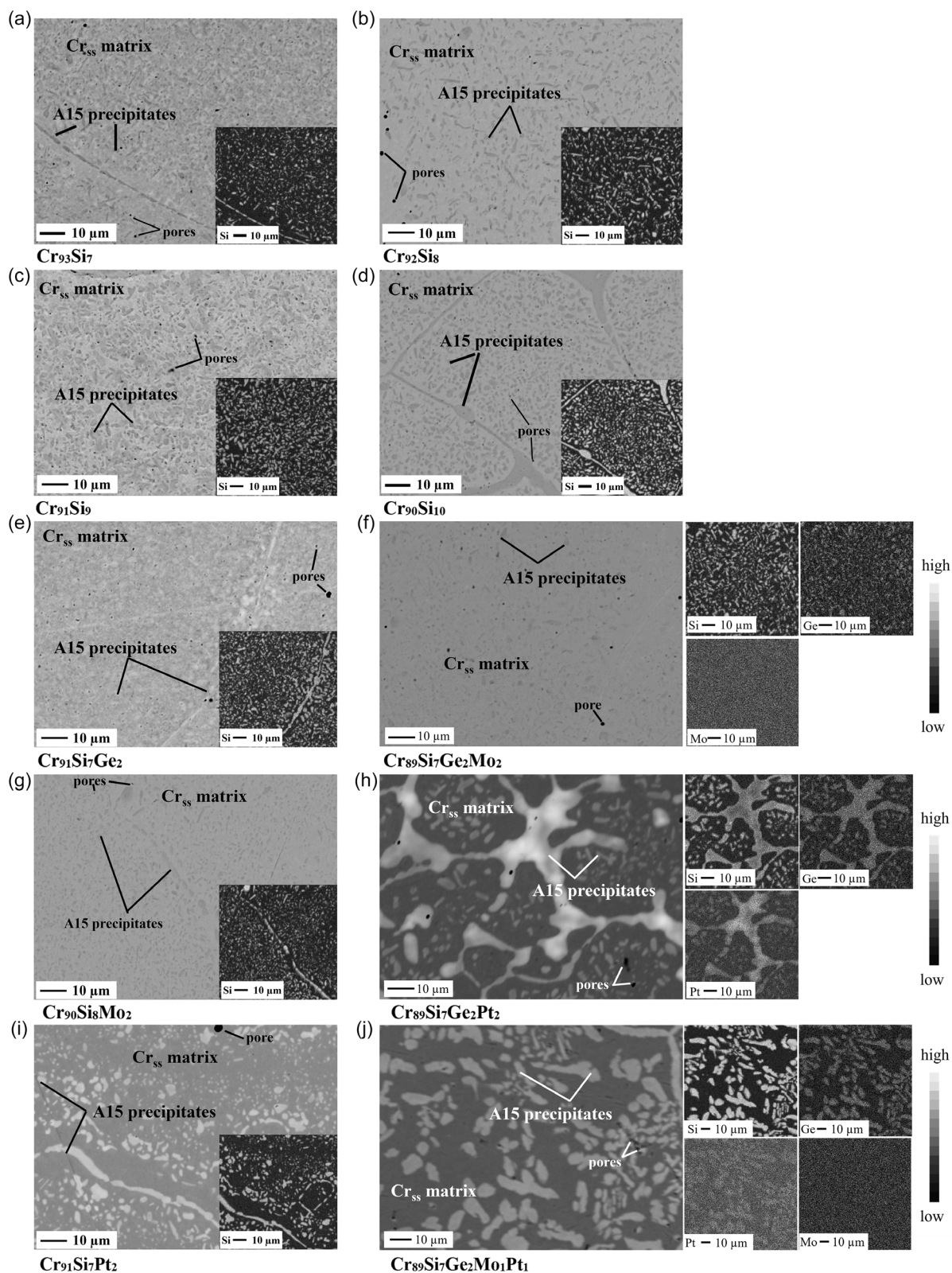**Figure 2.** Microstructures (BSE images) of the alloys after annealing for 100 h at 1200 °C of a) $Cr_{93}Si_7$, b) $Cr_{92}Si_8$, c) $Cr_{91}Si_9$, d) $Cr_{90}Si_{10}$, e) $Cr_{91}Si_7Ge_2$, f) $Cr_{89}Si_7Ge_2Mo_2$, g) $Cr_{90}Si_8Mo_2$, h) $Cr_{89}Si_7Ge_2Pt_2$, i) $Cr_{91}Si_7Pt_2$, and j) $Cr_{89}Si_7Ge_2Mo_1Pt_1$. are shown. Relevant EPMA element distribution maps are added to show the elemental partitioning and improve the viability of the Si-rich A15 phase.
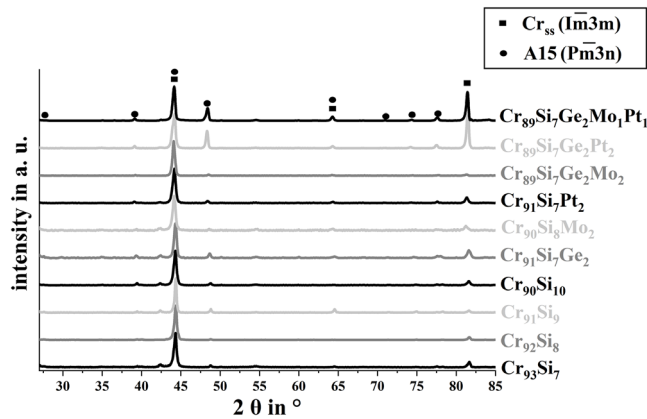
Figure 3. XRD diffraction patterns of the investigated alloys after heat treatment for 100 h at 1200 °C show a two-phase structure consisting of Cr_{ss} and A15 phases for all alloys. The measurements of $Cr_{91}Si_9$ and the ternary alloys were taken from a former study. Reproduced with permission.[15] Copyright 2024, Elsevier.

Considering the BSE images, the A15 phase appears comparably bright in the case of Pt addition, as Pt is a heavy element showing a higher concentration in the A15 phase compared to the Cr_{ss}. In contrast to this, the A15 phase appears comparably dark in the cases of adding lighter A15 phase forming elements such as Si and Ge. Enhanced variations in contrast in the A15 phase (e.g., Figure 2h) are attributed to segregations, which are more pronounced in alloys containing 2 at% Pt. In addition, pores form during arc melting with an area fraction of around 0.5%.[23,29]

Microstructures differ in A15-phase fraction and appearance. For example, the precipitates appear larger in Figure 2b,d,h,i than in other alloys. This effect is investigated in more detail after discussing elemental partitioning and its dependence on alloy composition.

On some microstructures, rather large and longitudinal A15-phase areas are detectable, which are aligned along the grain boundaries. These primary precipitates form after arc melting, while the more diminutive precipitates form during annealing.

Figure 3 shows the corresponding XRD measurements of the alloys. As already labeled in Figure 2, solely two phases form in all investigated compositions as proven by the XRD pattern: the Cr_{ss} matrix and A15-precipitates. Depending on the alloy's composition, the lattice parameters a_{Crss} and a_{A15} of the cubic phases slightly change.

In addition, the composition of both formed phases is investigated by quantitative measurements which are summarized in **Table 2**. It is found that the concentration of Si, Ge, and Pt increased in the A15 phase while Mo is found in comparable concentrations in both phases. For both phases, A15 and Cr_{ss}, the lattice parameters are determined from the XRD measurements shown in Figure 3 using the NR extrapolation function and added to Table 2.

To visualize the elemental partitioning, the mean k-factor, determined for each element considering all alloys, is given

Table 2. Phase compositions after heat treatment for 100 h at 1200 °C were measured using quantitative EPMA/.WDS analysis. The measurements of the binary and ternary alloys were taken from an earlier study. Reproduced with permission.[15] Copyright 2024, Elsevier. The lattice parameters of the respective cubic phases were determined from the XRD patterns using the NR extrapolation function.[32]

Alloy	Phase	c(Cr) in at%	c(Si) in at%	c(Ge) in at%	c(Mo) in at%	c(Pt) in at%	Lattice parameter in pm
$Cr_{93}Si_7$	Cr_{ss}	94.9 ± 0.4	4.9 ± 0.4	–	–	–	288.558
	A15	79.1 ± 0.7	20.9 ± 0.7	–	–	–	456.258
$Cr_{92}Si_8$	Cr_{ss}	94.8 ± 0.6	5.0 ± 0.5	–	–	–	288.493
	A15	79.0 ± 0.6	21.0 ± 0.6	–	–	–	456.258
$Cr_{91}Si_9$	Cr_{ss}	95.2 ± 0.6	4.8 ± 0.6	–	–	–	288.566
	A15	79.7 ± 0.2	20.3 ± 0.2	–	–	–	456.433
$Cr_{90}Si_{10}$	Cr_{ss}	94.1 ± 0.7	5.8 ± 0.7	–	–	–	288.663
	A15	78.9 ± 1.1	21.0 ± 1.1	–	–	–	456.399
$Cr_{91}Si_7Ge_2$	Cr_{ss}	94.8 ± 0.4	3.9 ± 0.4	1.3 ± 0.1	–	–	288.704
	A15	80.2 ± 0.6	15.1 ± 0.6	4.7 ± 0.8	–	–	457.870
$Cr_{90}Si_8Mo_2$	Cr_{ss}	92.5 ± 0.5	5.2 ± 0.5	–	2.0 ± 0.1	–	289.894
	A15	76.2 ± 1.2	21.7 ± 1.3	–	2.0 ± 0.1	–	458.000
$Cr_{91}Si_7Pt_2$	Cr_{ss}	92.9 ± 0.4	4.8 ± 0.2	–	–	1.9 ± 0.2	289.513
	A15	78.8 ± 0.4	17.6 ± 0.8	–	–	3.2 ± 0.4	459.884
$Cr_{89}Si_7Ge_2Mo_2$	Cr_{ss}	92.7 ± 0.5	4.0 ± 0.4	1.2 ± 0.1	2.0 ± 0.1	–	289.558
	A15	77.3 ± 1.0	16.6 ± 0.6	4.0 ± 0.4	2.0 ± 0.1	–	458.893
$Cr_{89}Si_7Ge_2Pt_2$	Cr_{ss}	93.5 ± 0.7	3.6 ± 0.3	1.2 ± 0.1	–	1.4 ± 0.1	289.351
	A15	78.9 ± 0.4	12.7 ± 1.3	4.3 ± 0.4	–	3.9 ± 0.7	460.155
$Cr_{89}Si_7Ge_2Mo_1Pt_1$	Cr_{ss}	93.3 ± 0.4	3.6 ± 0.3	1.2 ± 0.1	1.0 ± 0.1	0.9 ± 0.1	289.400
	A15	77.5 ± 0.3	15.4 ± 0.3	4.6 ± 0.3	1.1 ± 0.1	1.5 ± 0.1	459.806

in **Figure 4**a. $k(E)$ is calculated for each element E using Equation (1).

$$k(E) = \frac{c_{A15}(E)}{c_{Cr_{ss}}(E)} \tag{1}$$

It becomes evident that Si, Ge, and Pt all have higher concentrations in the A15 phase. Hence, these elements are A15-phase formers, while Mo shows no clear preference independent of the overall alloy composition. The elements Cr, Si, Ge, and Mo show relatively slight deviations in partitioning, but the partitioning of Pt highly depends on other alloying elements. While $k(Pt)$ is around 1.7 for $Cr_{91}Si_7Pt_2$ and $Cr_{89}Si_7Ge_2Mo_1Pt_1$, much higher k-factors are obtained for the composition $Cr_{89}Si_7Ge_2Pt_2$.

A Si_{eq} of Ge and Pt is determined by the partitioning results, resulting in the following equation.

$$Si_{eq} = Si + 0.89Ge + 0.51Pt \tag{2}$$

The elemental concentrations are considered in at%. Even though the equivalent for Pt depends on the overall alloy composition, the proposed Si_{eq} appears to be a valid approximation with respect to the studied Cr-rich Cr-Si alloys.

In Figure 4b, the A15-phase fractions are displayed over Si_{eq}. The values are listed in the Table S5, Supporting Information. The error of Si_{eq} is determined by the propagation of uncertainty and the measurements listed in Table 2. Figure 4b shows an increased A15-phase fraction with increasing Si_{eq}. Additionally, the solubility limit of Si in Cr_{ss} (see Table 2) related to an A15-phase fraction of zero is included, demonstrating a linear dependence between Si_{eq} and the A15-phase fraction.

3.2. Dimensions of A15 Precipitates and Grains

Comparing the microstructures of the alloys shown in Figure 2, a difference in A15 precipitate sizes formed of the different compositions is noticeable after annealing. To investigate this phenomenon, the precipitate's sizes were determined for all alloy compositions after annealing for 100 h at 1200 °C, as shown in **Figure 5**a. Therefore, the area of the precipitates is considered. Only the small, secondary precipitates are considered as they form and grow during the annealing step (starting diameter is 0), and therefore, their growth could be investigated.

Different statistic measures are the mean value, the median, and an interquartile range A of 25–75%; hence, 25–75% of the A15 precipitate lie in this range. Whiskers show the range of precipitate dimensions covering 5–95% of the precipitates, while outliers are added.

With increasing A15-phase former concentration in the alloy, a slight tendency for increasing A15 precipitates is visible. This is mainly observed for the binary alloys. However, the $Cr_{90}Si_{10}$ slightly deviates. A higher sum of the A15-phase former is also found for this alloy. Hence, it could be assumed that the microstructure of $Cr_{90}Si_{10}$ was not that close to thermodynamic equilibrium after annealing for 100 h at 1200 °C as the other binary alloys.

A tendency for an increase in precipitate sizes is also found with increasing the number of different A15-phase formers in the alloy. At 1200 °C, all quaternary alloys show the biggest precipitates, with $Cr_{89}Si_7Ge_2Pt_2$ showing outstanding high A15-precipitate dimensions. The precipitate dimensions of the ternary compositions appear quite comparable and are between the binary and quaternary alloys. The sum of A15-phase forming elements in Cr_{ss} (Figure 5b) slightly varies between the alloys without Pt; however, in the Pt-alloying case, the sum increases, especially for the $Cr_{91}Si_7Pt_2$ alloy.

Besides longer annealing times, temperature variations can be used to investigate the coarsening. To examine the effect of Mo and Ge in more detail, selected alloys were annealed for 400 h at 1050 °C and 100 h at 1350 °C. All these investigated alloys maintained their two-phase structure in this temperature range with slight deviations in phase composition. The microstructures (Figure S1, Supporting Information) and measured compositions and elemental partitioning (Table S1–S4 and Figure S2, Supporting Information) are added in the Supporting
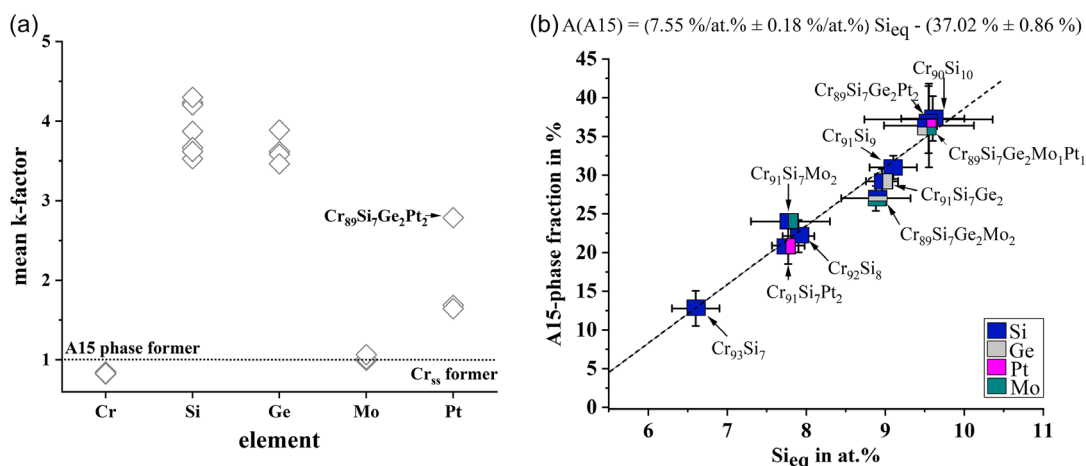

Figure 4. a) Elemental partitioning displayed by $k(E)$ calculated on the data shown in Table 2. b) A15-phase fraction over the Si_{eq}. All values refer to the microstructure after 100 h at 1200 °C annealing. The partitioning of ternary alloys was investigated earlier; however, in this study, the obtained values are supplemented by the new investigations considering quaternary and quinary alloys.
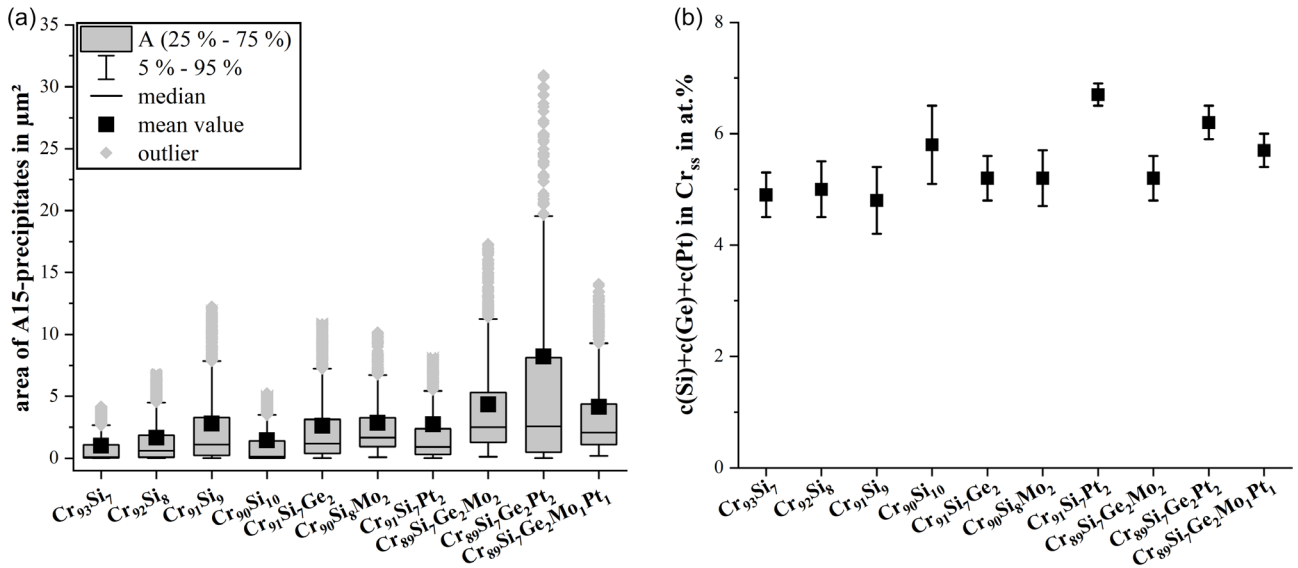
Figure 5. a) The dimensions of the A15 precipitates are given by the particle area determined after 100 h at 1200 °C annealing. b) The precipitate sizes are related to the sum of the A15 phase former in Cr_{ss}, which is $c(Si) + c(Ge) + c(Pt)$. The concentrations for 1200 °C are listed in Table 2.
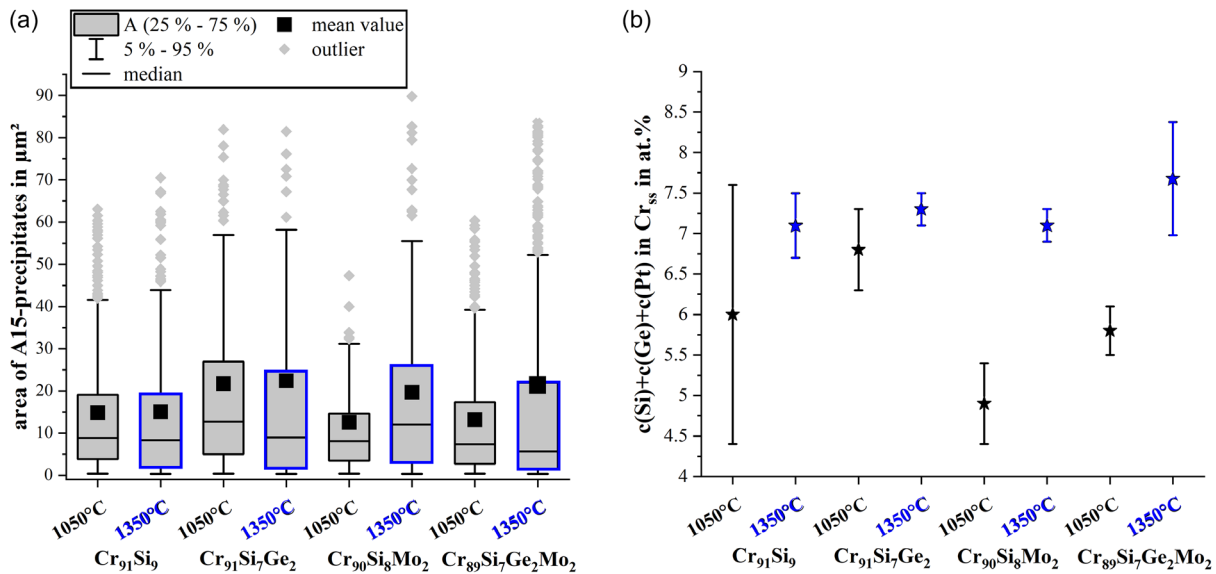

Figure 6. a) A15 precipitate dimensions given as area fraction and determined using image analysis. Several statistical values are shown for the A15 precipitate size evolution after annealing for 400 h at 1050 °C (marked with 1050 °C) and after annealing for 100 h at 1350 °C (marked with 1350 °C). b) The sum of the A15-phase former Si, Ge, and Pt measured in Cr_{ss}. The values can be found in the Supporting Information listed in Table S3 and S4.

Information of this paper. The results in precipitate dimensions are shown in **Figure 6**a, again referring to the precipitate area and to the small secondary precipitates that form during annealing.

After 400 h of annealing at 1050 °C, the Mo-containing alloys form the finest and most homogeneous in size A15 precipitates. Adding Mo to Ge also counteracts the increased coarsening obtained for the ternary $Cr_{91}Si_7Ge_2$ alloy. This effect can be correlated to the decrease in A15-phase formers dissolved in Cr_{ss} in the Mo-containing alloys. At 1350 °C, the trend of increased

A15-precipitate dimensions with increasing alloy complexity was also found. As shown in Figure 6b, the concentration of A15-phase forming elements dissolved in Cr_{ss} at 1350 °C is comparable to that of all alloy compositions after 100 h of annealing. However, the ternary and the quaternary alloys were found to form bigger A15 precipitates.

In addition, the grain size of the investigated alloys is measured using EBSD; the values are listed in **Table 3**. The solidification after arc melting causes the formation of anisotropic

Table 3. Grain sizes of the alloy annealed for 100 h at 1200 °C.

Alloy	Average grain size assuming equiaxed grains in μm	Average grain size major axis in μm	Average grain size minor axis in μm
$Cr_{91}Si_9$	127.4 ± 35.9	107.7 ± 22.3	41.1 ± 10.4
$Cr_{91}Si_7Ge_2$	88.0 ± 39.2	71.0 ± 28.0	23.1 ± 1.0
$Cr_{90}Si_8Mo_2$	107.4 ± 30.1	80.3 ± 25.3	33.8 ± 9.1
$Cr_{91}Si_7Pt_2$	92.6 ± 39.5	65.5 ± 29.1	31.3 ± 11.6
$Cr_{89}Si_7Ge_2Mo_2$	42.9 ± 28.0	33.01 ± 23.67	12.74 ± 7.20
$Cr_{89}Si_7Ge_2Pt_2$	66.1 ± 33.4	53.0 ± 30.7	21.2 ± 9.5
$Cr_{89}Si_7Ge_2Mo_1Pt_1$	84.7 ± 61.9	70.4 ± 22.1	22.1 ± 14.7

grains with a preferred direction of solidification. Therefore, the grain diameter in the minor and major axis and the orientation offset are given. The grain size measurements in Table 3 show comparable large, rather longitudinal grains for $Cr_{91}Si_9$ and $Cr_{90}Si_8Mo_2$. The grain size decreases with the addition of other elements and with a more complex composition while maintaining their longitudinal shape from the melting process. No significant differences between all Pt-containing alloys are found. Considering the Cohen effect size, the quaternary alloy $Cr_{89}Si_7Ge_2Mo_2$ shows significantly smaller and the ternary $Cr_{90}Si_8Mo_2$ significantly larger grains than the Pt-containing alloys.

3.3. Hardness Measurements

In **Figure 7**, the results of the hardness measurements are shown. The A15 phase is found to be harder compared to the solid solution. Concerning the measurement errors, the hardness of the A15 phase is comparable, and a trend in the alloying elements is hard to extract. Exceptions are lower hardnesses

measured for alloys containing 8 at% Si. The hardness of the Cr_{ss} is found to go well with the total amount of alloying elements in Cr_{ss} ($c(Si) + c(Ge) + c(Mo) + c(Pt)$) in Cr_{ss} from Table 2). Slight deviations toward a higher hardness of the Cr_{ss} are found when combining Ge and Pt in the alloy.

In addition, microhardness measurements considering the combined hardness of the Cr_{ss} matrix and A15 precipitates of all alloys were conducted, combining the effects of alloying elements on both phases. The results are shown in Figure 7b depending on the A15-phase fraction. The microhardness of the alloys increases with increasing the phase fraction of the harder A15 phase.

The following effects of alloying elements are found: All alloy compositions either maintain or increase the hardness compared to the binary systems assuming constant A15-phase fractions. As the hardness of the A15 phase is (with two exceptions) independent of alloy composition with respect to the measurement errors (Figure 7a), the change in microhardness of the ternary, quaternary, and quinary alloys is mainly attributed to the elemental effects on solid solution hardening of the Cr_{ss} matrix. Concerning the ternaries, Pt increases the alloy's hardness most significantly from HV0.3 414 ($Cr_{92}Si_8$) to HV0.3 541 ($Cr_{91}Si_7Pt_2$) due to an increased hardness of the Cr_{ss} matrix of 10.4 GPa ($Cr_{91}Si_7Pt_2$) compared to 7.7 GPa ($Cr_{92}Si_8$). The increase is 31% and 39%, respectively, which fits into the range of increased solubility of A15-phase former in the Cr_{ss} matrix ($\approx 34\%$, compared to Table 2). In **Table 4**, the percent values of the increase in hardness and dissolved elemental concentrations in Cr_{ss} are given, as well as the binary alloys which were taken as reference.

The increase of the Vickers hardness, nanohardness of Cr_{ss}, and concentration of dissolved elements in Cr_{ss} of $Cr_{91}Si_7Ge_2$, $Cr_{91}Si_7Pt_2$, and $Cr_{89}Si_7Ge_2Pt_2$ are comparable. In contrast to this, all Mo-containing alloys show a deviation from solid solution hardening and the measured nanohardness and microhardness. For the ternary $Cr_{90}Si_8Mo_2$ alloy, the hardness of Cr_{ss} still fits the concentration of dissolved elements, but Vicker's hardness is
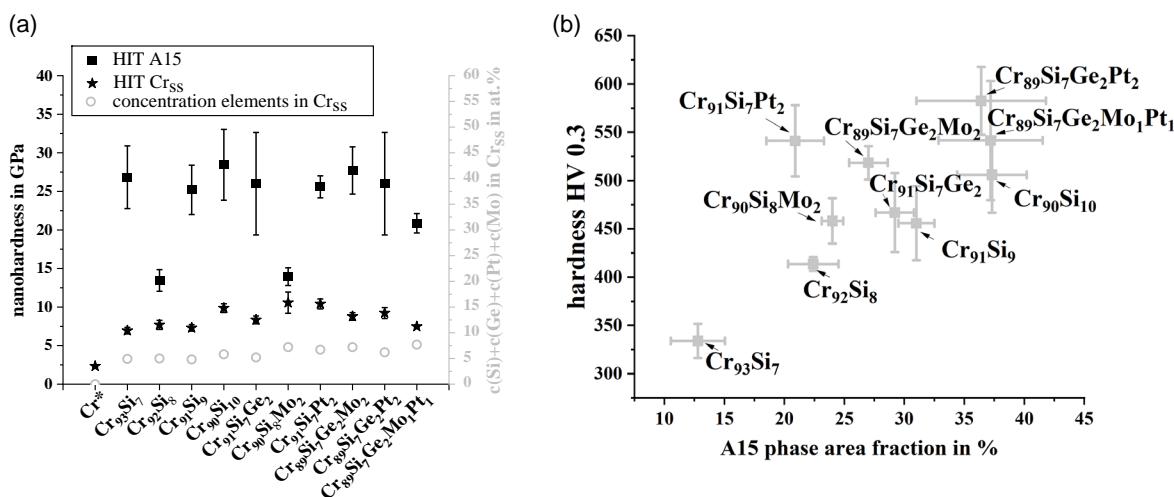

Figure 7. a) The nanohardness measurements of the Cr_{ss} matrix and the A15 phase are correlated to the alloys and the A15-phase former concentration in the Cr_{ss} (right y-axis). In addition, a measurement for pure Cr is added from another study. ($*^{[39]}$) The values can be found in Table S6 in the Supporting Information. b) Microhardness measurements using the Vickers hardness test are correlated to the A15-phase fraction. The values for the binary and ternary alloys were taken from an earlier study to complete the overall behavior. Reproduced with permission[15] Copyright 2024, Elsevier.

Table 4. Percent values for the increase in hardness and concentrations of dissolved elements in Cr$_{ss}$ determined with respect to the named binary reference alloys.

Alloy	Increase vickers hardness in %	Increase nanohardness of Cr$_{ss}$ in %	$c(Si) + c(Ge) + c(Pt) + c(Mo)$ in Cr$_{ss}$ in %	Reference alloy
Cr$_{91}$Si$_7$Ge$_2$	13	13	8	Cr$_{91}$Si$_9$
Cr$_{91}$Si$_7$Pt$_2$	31	39	34	Cr$_{92}$Si$_8$
Cr$_{91}$Si$_8$Mo$_2$	11	38	44	Cr$_{92}$Si$_8$
Cr$_{89}$Si$_7$Ge$_2$Pt$_2$	28	26	29	Cr$_{91}$Si$_9$
Cr$_{89}$Si$_7$Ge$_2$Mo$_2$	20	14	50	Cr$_{91}$Si$_9$
Cr$_{89}$Si$_7$Ge$_2$Pt$_1$Mo$_1$	19	2	60	Cr$_{91}$Si$_9$

much lower. The more complex compositions show also a lower hardness increase with respect to the expected solid solution hardening.

4. Discussion

4.1. Elemental Phase Partitioning and Effect on Lattice Parameter Misfit

In all investigated ternary, quaternary, and quinary compositions, Si, Ge, and Pt were found to be A15-phase former, while Mo was found to show a neutral partitioning to both phases (see Figure 4a). This finding is very interesting as it allows alloy design up to quinary composition spaces, which are usually hard to access by thermodynamic calculations using available databases. Even though Pt was found to show a partitioning highly depending on the total alloy composition, Equation (2) provides a reasonable Si$_{eq}$ for assessing the microstructure of Cr-rich Cr-Si alloys at 1200 and 1350 °C (compare Figure S2, Supporting Information). The metallic or covalent (covalent marked with *) radii (Si*: 116 pm, Cr: 128 pm, Ge*: 121 pm, Mo: 139 pm, Pt: 138 pm) of the alloying elements are in all cases bigger compared to the reference binary system.[35] In solid solution, the lattice parameters are shifted toward higher values in the ternary, quaternary, and quinary alloys.

In all cases, the shift of lattice parameters of the respective phases is positive when adding additional alloying elements (compare Table 1). Tarutani and Kudo determined the lattice parameters of the elements in the A15-phases.[36] All alloying elements' atomic radii are bigger than Si and Cr (Si: 124 pm, Cr: 129 pm, Ge: 130 pm, Pt: 139 pm, Mo: 140 pm), which explains the found shifts.

The lattice parameter misfits Δm_f were determined using the following orientation relationships (OR), which were previously reported for binary and Cr-Si-Pt ternary Cr-Si alloys

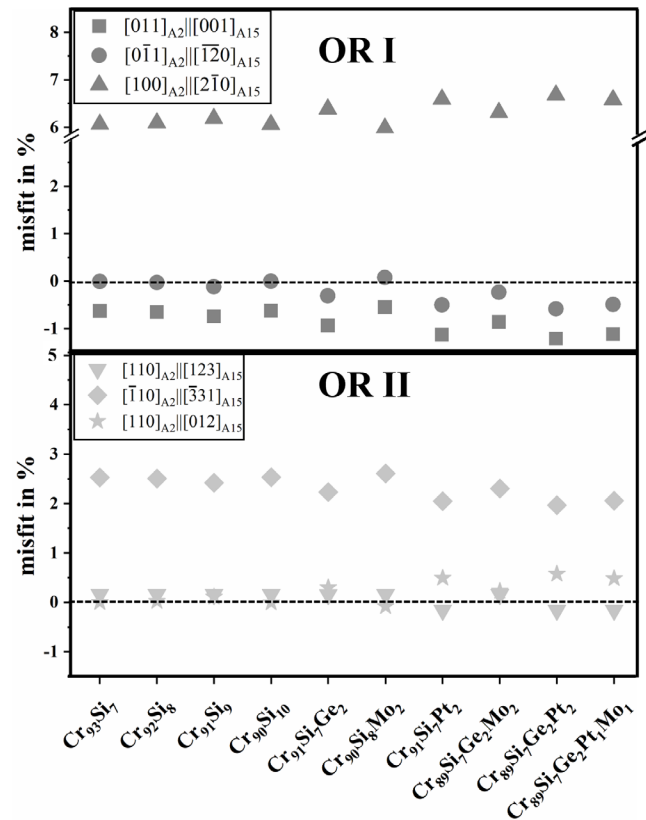| OR I:[18,37]	OR II:[18,38]
$[011]_{A2}\|[001]_{A15}$	$(011)_2\|(012)_{A15}$
$[0\bar{1}1]_{A2}\|[\bar{1}20]_{15}$	$(\bar{1}10)_{A2}\|(\bar{3}31)_{A15}$
$[200]_{A2}\|[2\bar{1}0]_{A15}$	

Figure 8. Lattice parameter misfit between the Cr$_{ss}$ matrix and A15 precipitates determined concerning the two reported orientation relationships (OR I and OR II) and the experimentally determined lattice parameters (see Table 1).

For both ORs Δm_f is shown in **Figure 8** based on the following calculation

$$\Delta m_f = (b - c)/c \qquad (3)$$

Based on the identification of the parallel planes in Cr$_{ss}$ and A15, the respective atomic distances in these planes were determined to be b for the A15 phase and c for the Cr$_{ss}$ matrix phase. From the longitudinal appearance of the A15-precipitates formed in the alloys in Figure 2, the impression appears that the misfit in lattice parameters is plane dependent. This impression is supported by the determined misfits for the two ORs, which show high deviations in misfits depending on the respective orientation of both phases (see Figure 8).

The precipitates were found to be semicoherent. The orientation relationship and alloy composition influence the coherence. The binary alloys and Cr$_{90}$Si$_8$Mo$_2$ show the overall lowest misfits. Cr$_{91}$Si$_7$Ge$_2$ only slightly increases the misfit. The Cr-Si-Ge-Mo quaternary alloy is in between both ternary alloys. In contrast to these relatively low changes, Pt significantly impacts the misfit by increasing it for all Pt-containing alloys. This is attributed to the increase of the A15-phase lattice parameter.

ADVANCED
SCIENCE NEWS

www.advancedsciencenews.com

ADVANCED
ENGINEERING
MATERIALS

www.aem-journal.com

4.2. Stability of Microstructure and Dependence on Alloy Composition

A coarsening rate can describe the stability of the microstructure concerning precipitate formation. The coarsening rate increases with annealing time t, elemental diffusion expressed by the diffusion coefficient D, the specific enthalpy γ_{in} of the Cr_{ss}/A15 interface, and the solubility of A15-precipitate forming elements in the matrix c_0. Diffusion exponentially depends on temperature. Hence, an increase in the A15-precipitate size is found in Figure 5b, even though the annealing time is quadrupled. Further comparisons between the alloys refer to the same annealing conditions. For the binary alloys, the effect of diffusion is found indirectly with an increasing A15-precipitate size over increasing A15-phase fraction. An increasing A15-phase fraction causes a decrease in precipitate distance, which enhances the growth of bigger precipitates.

As shown in Figure 5 and 6, the tendency of increased concentration of A15-phase former ($c(Si) + c(Pt) + c(Ge)$) solubility limit c_0 in the solid solution also increases the A15 precipitate sizes. Hence, the coarsening of the A15-phases increases with an increasing number of different A15-phase formers in the alloy and an increase in dissolved A15-phase formers in the solid solution. However, the Pt-containing alloys stand out from the trend. Recently, the mechanism of the increased microstructural coarsening by Pt addition was investigated by comparing the compositions $Cr_{91}Si_9$, $Cr_{91}Si_7Pt_2$, and $Cr_{86}Si_8Pt_6$ with the conclusion, that the highest effect on the increased coarsening by Pt addition is attributed to a thermodynamic destabilization of the interface.[18] The enhanced lattice parameter misfit, supported by the current findings, plays a less pronounced role. The theory of a Pt enrichment at the Cr_{ss}/A15-phase interface being the highest driving force for A15-phase coarsening is also supported in this study. As shown in Figure 5, the A15 precipitates of the alloys containing 2 at% Pt deviate most from the A15 precipitate sizes of the other alloys. The alloy with only 1 at% Pt demonstrates a better fit to the alloys without Pt. In addition, the partitioning of Pt was found to have a considerable deviation depending on the overall alloy composition (see Figure 4a). This compositional variance is already visible in the micrographs shown in Figure 2i,h.

Concerning Mo additions, the $Cr_{90}Si_8Mo_2$ alloy annealed for 400 h at 1050 °C was found to form comparable fine and homogeneous distributed A15-precipitates. This can be attributed to the decreased sum of A15-phase forming elements dissolved in Cr_{ss} at 1050 °C (see Figure 6). For the other alloys containing Mo and Ge, c_0 lies in the same range, and the deviations in A15 precipitate sizes have to be attributed to the specific enthalpy γ_{in} of the Cr_{ss}/A15 interface. This enthalpy increases with the increase in the misfit of the lattice parameters. This was higher for ternary and quaternary alloys than the binary system (see Figure 5 and 6). For example, for annealing at 1350 °C, the ranking of the smallest A15-precipitate size concerning the mean value is $Cr_{91}Si_9 < Cr_{90}Si_8Mo_2 < Cr_{91}Si_7Ge_2 < Cr_{89}Si_7Ge_2Mo_2$. This goes well with the change in lattice misfit (see Figure 8) and can be solely related to this; as all samples show a comparable concentration of A15-phase former in Cr_{ss} (see Table 2 and Table S3, S4, Supporting Information). Hence, all ternary,

quaternary, and quinary alloying increases the A15-precipitate size and, therefore, its coarsening rate compared to the binary alloys. However, Ge and Mo cause a much slighter increase compared to Pt. For Ge, this increase appears to be independent of temperature in the investigated range, which ranges from 1050 to 1350 °C. This increased microstructural coarsening by substituting Si with Ge agrees with former studies on different ternary compositions of $Cr_{84}(Ge_x,Si_{x-1})_{16}$ alloys annealed at 1350 °C.[22]

For Mo, the lower temperature maintains a fine and homogeneous distributed microstructure as the amount of dissolved elements in Cr_{ss} is decreased by Mo addition. Combining Mo and Ge and thereby the over A15-phase fraction, the precipitate sizes increase for the higher temperatures again, while at 1050 °C the low c_0 again limits the fast growth. Hence, especially for lower temperatures such as 1050 °C, low Mo additions can be used to counteract microstructural coarsening in Cr-rich Cr-Si alloys.

4.3. Elemental Effect on Hardness

In previous studies, pure Cr was found to have a hardness between 1.1 GPa and 2.33 GPa depending on the purity and the amount of grain boundaries.[39,40] The purity of the material in this study is in the range of the former studies, and the material is polycrystalline with grain sizes that are comparable to the material used in the previous studies and which obtained more than 2 GPa (grain size $\approx$35 μm, purity 99.8%).[39] Hence, in this study, it is shown that the hardness of the matrix phase increases significantly by solid solution hardening when alloyed with Si (see Figure 7a). This is even more obvious when the nanohardness of Cr_{ss} is correlated to the concentration of A15-phase former ($c(Si) + c(Ge) + c(Pt)$) dissolved in Cr_{ss}. Both values align perfectly telling of a strong correlation (see Table 4).

The measured Vickers hardnesses of the Cr-Si alloys also agree with the former studies. The values measured for the alloys lie between the hardness of pure Cr (HV0.2 $\approx$144, average grain size $\approx$653.1 μm) and the Cr_3Si A15-phase (HV0.3 $\approx$1200, no grain size given). The nanoindentations of the A15-phase show that the A15-phase is around three times harder than the Cr_{ss} matrix phase. Even though two alloys, $Cr_{92}Si_8$ and $Cr_{90}Si_8Mo_2$, stand out with a much-decreased A15-phase hardness, the microhardness measurements fit well with the linear dependence on A15-phase fraction (see Figure 6b).[37,41] Hence, the anomaly of measured A15-phase hardness must be attributed to an effect on the microscale that is superimposed on a macroscopic scale.

Mo-containing alloys show a deviation between dissolved elements in the solid solution and an increase in solid solution hardening (compare Table 4). With respect to the limited compositions investigated, no clear trend could be found. Recently, room temperature ductility was reported for a single-phase solid solution, $Cr_{51}Mo_{36}Si_3$ alloy, attributed to a deformation twinning mechanism and a large difference in lattice parameters between Cr and Mo.[28] If the change in hardness can be attributed to a similar change in deformation mechanism with Mo-addition from, for example, dislocation slip to deformation twinning has to be proven in the future.

Considering the grain size, $Cr_{91}Si_9$ and $Cr_{90}Si_8Mo_2$ were found to have the highest grain sizes. However, concerning the Vickers hardness measurements, the behavior shows no direct correlation to grain size. The explanation for this is straightforward because the Vickers indents have a size of around 20 μm. This value is below the average grain size (compare Table 3); therefore, the grain size plays a minor role in the measured hardness. Considering the sizes of the A15 precipitates (see Figure 5) and the measured Vickers hardness, the hardness increases with increased precipitate size. As it is known that the coarsening of precipitates decreases the material's hardness, the variations in hardness could not be related to the A15-phase coarsening. It is concluded that neither the A15 precipitate size nor the grain size defines the alloy's hardness determination in this study but rather the solid solution hardening of the Cr_{ss} matrix phase and the overall A15-phase fraction.

5. Conclusion

A binary BCC-A15 microstructure was found for Cr-rich Cr-Si alloys (Cr ≥ 89 at%) alloyed with Si, Ge, Pt, and Mo and annealed for 400 h at 1050 °C, 100 h at 1200 °C, and 100 h at 1350 °C.

The microstructural effects of the different alloying elements on A15-phase fraction, partitioning, microstructural stability, grain size, and hardness were described and, for example, room temperature hardness was shown to be dominated by the solid solution hardening of the Cr_{ss} matrix. The A15-phase fraction was correlated to Si_{eq} developed based on the partitioning behavior of individual elements. The contribution of each element with respect to the investigated alloy compositions can be summarized as follows.

5.1. Silicon

Si is the strongest A15-phase former. With increasing Si concentration, the A15-phase fraction and microhardness increase linearly in the investigated composition range. The microstructures of the binary Cr-Si alloys were found to be the most stable considering coarsening due to the lowest lattice mismatch and a comparable low solubility of Si in Cr_{ss} compared to the more complex systems.

5.2. Germanium

Ge acts as A15-phase former with a Si_{eq} of 0.89. It slightly increases the hardness of Cr_{ss} as it slightly increases the solubility c_0 of the A15-phase former in Cr_{ss}. However, the increase of c_0, in turn, affects the microstructural stability because the higher A15-phase former concentration in Cr_{ss} increases the coarsening rate. However, this is not the whole story as for 1350 °C, comparable c_0 concentrations to other alloys were found, but again a slightly increased size in A15 precipitates. Another reason is the larger misfit of the Cr_{ss} matrix and A15 precipitates which also causes an increase in microstructural coarsening by Ge addition.

5.3. Platinum

Among the investigated A15-phase former, Pt is the weakest. Its Si_{eq} is determined to be 0.51, leading to a good approximation for the investigated property correlations; however, its partitioning depends on the overall alloy composition. Pt is known to thermodynamically destabilize the Cr_{ss}/A15-phase interface because it segregates to the interface. These segregations are also visible in the A15-phase areas and lead to faster coarsening of the microstructures when alloyed with Pt. The increased segregation and coarsening can be counteracted by adding Mo, as was demonstrated for the quinary $Cr_{89}Si_7Ge_2Mo_1Pt_1$ alloy. In the absence of Mo, Pt was found to increase the hardness of the alloys, which is mainly attributed to an increased hardness in Cr_{ss}. Hence, Pt addition must be well balanced because of the increased coarsening.

5.4. Molybdenum

Mo shows mutual partitioning behavior in both solid solution and intermetallic A15 phase. Its effect on hardness is not as pronounced as in the case of Pt, but it also increases the hardness of Cr_{ss}. Mo-containing alloys tend to show a fine microstructure comparable to the Ge-containing alloys at 1200 and 1350 °C and can counteract the increased coarsening of Pt. At 1050 °C, the Mo-containing alloys stand out by the formation of much finer A15 precipitates compared to the binary $Cr_{91}Si_9$ alloy. The effect on the lattice mismatch of Mo was found to be neglectable. The effect of the decrease in A15 precipitate sizes is related to the decreased solubility limit of A15-phase forming elements in the Cr_{ss} by adding Mo.

More alloying elements are needed to optimize the mechanical properties of Cr-Si alloys. Mo, so far, is the most promising alloying element for the Cr-Si system.

Supporting Information

Supporting Information is available from the Wiley Online Library or from the author.

Conflict of Interest

The authors declare no conflict of interest.

**ADVANCED
SCIENCE NEWS**

www.advancedsciencenews.com

**ADVANCED
ENGINEERING
MATERIALS**

www.aem-journal.com

Author Contributions

Data Availability Statement

The data that support the findings of this study are available from the corresponding author upon reasonable request.

Keywords

[1] H. Cr-Si Okamoto, *JPE* **2001**, *22*, 593.

[2] K. Ioroi, I. Ohnuma, X. Xu, R. Kainuma, T. Omori, *Calphad* **2024**, *85*, 102690.

[3] A. S. Dorcheh, M. Galetz, *JOM* **2016**, *68*, 2793.

[4] G. A. Yakaboylu, K. Sabolsky, E. M. Sabolsky, *J. Alloys Compd.* **2018**, *769*, 430.

[5] Y. Aono, T. Omori, R. Kainuma, *Intermetallics* **2019**, *112*, 106526.

[6] P. Pfizenmaier, A. S. Ulrich, M. C. Galetz, U. Glatzel, *Intermetallics* **2020**, *116*, 106636.

[7] S. Zhao, Y. Zhong, Z. Li, L. Wu, X. Wu, Z. Ning, C. Liu, J. Yang, *Vacuum* **2023**, *218*, 112627.

[8] U. S. Geological Survey, Mineral Commodity Summaries 2024: U.S. Geological Survey, **2024**, p 58.

[9] European Commission, Study on the Critical Raw Materials for the EU 2023-Final Report.

[10] W. H. Smith, A. U. Seybolt, *J. Electrochem. Soc.* **1956**, *103*, 347.

[11] Y. F. Gu, H. Harada, Y. Ro, *J. Miner. Met. Mater. Soc.* **2004**, *56*, 28.

[12] K. Ioroi, Y. Aono, X. Xu, T. Omori, R. Kainuma, *J. Phase Equilib. Diffus.* **2022**, *43*, 229.

[13] L. Royer, S. Mathieu, C. Liebaut, P. Steinmetz, *MSF* **2008**, *595–598*, 1047.

[14] A. Bhowmik, H. T. Pang, I. M. Edmonds, C. M. Rae, H. J. Stone, *Intermetallics* **2013**, *32*, 373.

[15] A. S. Ulrich, P. Pfizenmaier, A. Solimani, U. Glatzel, M. C. Galetz, *Int. J. Refract. Met. Hard Mater.* **2018**, *76*, 72.

[16] L. Pandelaers, R. Schmid-Fetzer, in *Chromium - Molybdenum - Silicon, Landolt Börnstein - Group IV Physical Chemistry*, Springer-Verlag, Berlin, Heidelberg **2010**, p. 182.

[17] A. Berche, J. C. Tédenac, P. Jund, *Calphad* **2015**, *49*, 50.

[18] A. S. Ulrich, A. J. Knowles, V. Cantatore, A. Bhowmik, M. T. Wharmby, C. Geers, I. Panas, M. C. Galetz, *Mater. Design* **2022**, *218*, 110655.

[19] B. V. Cockeram, G. Wang, R. A. Rapp, *Mater. Corros.* **1995**, *46*, 207.

[20] Y.-R. He, R. A. Rapp, P. P. Tortorelli, *Mater. Sci. Eng.: A* **1997**, *222*, 109.

[21] A. Soleimani Dorcheh, M. C. Galetz, *Oxid. Met.* **2017**, *88*, 549.

[22] A. S. Dorcheh, W. Donner, M. C. Galetz, *Intermetallics* **2018**, *93*, 201.

[23] M. Ouardi, *Master Thesis*, University of Bayreuth, Bayreuth **2024**.

[24] L. Koliotassis, E. M. H. White, M. C. Galetz, *Adv. Eng. Mater.* **2024**, *26*, 2301906.

[25] A. S. Ulrich, P. Pfizenmaier, A. Solimani, U. Glatzel, M. C. Galetz, *Corros. Sci.* **2020**, *165*, 108376.

[26] F. Hinrichs, A. Kauffmann, A. S. Tirunilai, D. Schliephake, B. Beichert, G. Winkens, K. Beck, A. S. Ulrich, M. C. Galetz, Z. Long, *Corros. Sci.* **2022**, *207*, 110566.

[27] P. Pfizenmaier, A. S. Ulrich, M. Galetz, U. Glatzel, *Metals* **2021**, *11*, 1072.

[28] F. Hinrichs, G. Winkens, L. K. Kramer, D. Schliephake, G. Falcão, M. C. Galetz, H. Inui, A. Kauffmann, M. Heilmaier, *Overcoming Barriers for High Temperature Alloys: Oxidation and Ductility*, Karlsruher Institut für Technologie, **2024**.

[29] K. Müller, *Master Thesis*, Universität Bayreuth, Bayreuth **2024**.

[30] A. S. Ulrich, *Dissertation*, Universität Bayreuth, Bayreuth **2020**.

[31] E. Rudy, H. Nowotny, *Monatsh. Chem.* **1974**, *105*, 156.

[32] J. B. Nelson, D. P. Riley, *Proc. Phys. Soc.* **1945**, *57*, 160.

[33] C. A. Schneider, W. S. Rasband, K. W. Eliceiri, *Nat. Methods* **2012**, *9*, 671.

[34] A. C. Fischer-Cripps, *Surf. Coat. Technol.* **2006**, *200*, 4153.

[35] J. C. Slater, *J. Chem. Phys.* **1964**, *41*, 3199.

[36] Y. Tarutani, M. Kudo, *J. Less Common Met.* **1977**, *55*, 221.

[37] H. Bei, E. P. George, E. A. Kenik, G. M. Pharr, *Acta Mater.* **2003**, *51*, 6241.

[38] B. P. Bewlay, J. A. Sutliff, M. R. Jackson, K. M. Chang, *Mater. Manufact. Process.* **1994**, *9*, 89.

[39] C. Brandl, I.-C. Choi, R. Schwaiger, *Mater. Sci. Eng.: A* **2022**, *852*, 143629.

[40] V. Maier, A. Hohenwarter, R. Pippan, D. Kiener, *Scr. Mater.* **2015**, *106*, 42.

[41] D. Terentyev, T. Khvan, J.-H. You, N. Van Steenberge, *J. Nucl. Mater.* **2020**, *536*, 152204.

2401818 (12 of 12)